Measurements and 2-D modeling of recycling and edge transport in discharges with lithium-coated PFCs in NSTX

J.M. Canik [a],[*],[1], R. Maingi [a], V.A. Soukhanovskii [b], R.E. Bell [c], H.W. Kugel [c], B.P. LeBlanc [c], T.H. Osborne [d]

[a] Oak Ridge National Laboratory, Oak Ridge, TN, USA
[b] Lawrence Livermore National Laboratory, Livermore, CA, USA
[c] Princeton Plasma Physics Laboratory, Princeton, NJ, USA
[d] General Atomics, San Diego, CA, USA

ARTICLE INFO

Article history:
Available online 2 December 2010

ABSTRACT

The application of lithium coatings on plasma facing components has been shown to profoundly affect plasma performance in the National Spherical Torus Experiment, improving energy confinement and eliminating edge-localized modes. The edge particle balance during these ELM-free discharges has been studied through 2-D plasma-neutrals modeling, constrained by measurements of the upstream plasma density and temperature profiles and the divertor heat flux and D_α emission. The calculations indicate that the reduction in divertor D_α emission with lithium coatings applied is consistent with a drop in recycling coefficient from $R \sim 0.98$ to $R \sim 0.9$. The change in recycling is not sufficient to account for the change in edge density profiles: interpretive modeling indicates similar transport coefficients within the edge transport barrier ($D/\chi_e \sim 0.2/1.0 \ \mathrm{m^2/s}$), but a widening of the barrier with lithium.

© 2010 Elsevier B.V. All rights reserved.

1. Introduction

Lithium has gained attention as a candidate plasma facing material for fusion reactors [1], due to strongly pumping hydrogenic species [2] and possibly improving energy confinement (τ_E) [3–5]. Lithium is being used in plasma facing components (PFCs) in several experiments, both as a solid [6] and as a liquid [7]. The ability of lithium coatings to provide pumping in a diverted tokamak configuration is being tested in the National Spherical Torus Experiment [8]. These coatings are applied to carbon PFCs using a pair of lithium evaporators [9] that preferentially coat the lower divertor region.

Lithium coating of the NSTX PFCs significantly affects plasma performance. When applied, τ_E improves, mainly in the electron channel [10] (due to a broadening of the temperature profile [11]). ELM behavior is also strongly impacted. During conventional H-mode operation, ELMs are routinely observed in NSTX [12]. However, with sufficient deposition of lithium, ELMs are entirely eliminated [13]. This is attributed to an inward shift of the pedestal density profile and reduction of its gradient. This gives an inward shift of the peak pedestal pressure gradient, reducing the drive for peeling–ballooning modes [14].

This paper describes 2-D interpretive modeling of two discharges, one an ELMy plasma with boronized carbon PFCs (referred to as the "pre-lithium" case), the other a companion ELM-free discharge with lithium ("post-lithium" case). The modeling is constrained by experimental measurements, providing a method for determining the PFC recycling and cross-field transport coefficients, in order to quantify the effects of lithium coating of the PFCs.

2. Interpretive modeling of NSTX discharges

The two plasmas under consideration had similar global parameters, with plasma current, magnetic field, elongation and triangularity of 800 kA, 0.5 T, 1.9 and 0.5, respectively. The plasma stored energy in these discharges was matched, with $W_{MHD} \sim 170$ kJ during the H-mode phase studied here. Due to increased τ_E, however, the input power from neutral beam injection was reduced from $P_{NBI} \sim 4$ MW without lithium to ~ 2 MW with lithium (this was necessary to avoid global stability limits [14]). Core profiles of density and temperature can be found in Ref. [14].

Modeling was performed using the SOLPS suite of codes [15], which couples the 2-D fluid plasma transport code B2.5 [16] with the EIRENE Monte Carlo neutrals code [17]. This gives a self-consistent calculation of transport through the pedestal and scrape-off-layer (SOL), including the neutral contributions due to recycling. Transport is treated as classical parallel to the magnetic field (with corrections for kinetic effects), and in the cross-field direction is governed by user-specified transport coefficients. At the inner simulation boundary, located at normalized poloidal flux $\psi_N \sim 0.8$, the heating power from experiment is input as a

* Corresponding author. Address: 1 Bethel Valley Rd., Oak Ridge, TN 37831, USA.
  E-mail address: canikjm@ornl.gov (J.M. Canik).
[1] Presenting author.

boundary condition. Similarly, the particle flux at the inner boundary is set to match the particle fueling from neutral beam injection. Gas puffing from a valve located on the center column is included. Plasma flux that leaves the grid across the last radial grid surface is recycled as neutrals, and neutral recycling from the main chamber wall is included in EIRENE.

The cross-field transport coefficients for each case are determined by fitting the midplane temperature and density profiles from the simulations to those measured experimentally using Thomson scattering and charge exchange recombination spectroscopy. This is done iteratively as follows. First, an initial guess for D, χ_e, and χ_i is taken, with values independent of radius, and the simulation is run a few hundred iterations with a time step $\Delta t \sim 10^{-5}$–10^{-6} s. Then the profiles of the radial electron and ion heat and particle fluxes are taken from the code along a 1-D slice at constant poloidal angle, through the outer midplane of the plasma. The code fluxes are combined with the experimental profiles to calculate a new set of coefficients according to

$$D^{new} = -\Gamma^{SOLPS}/\nabla n^{EXP}$$
$$\chi_{e,i}^{new} = -\left(q_{e,i}^{SOLPS} - \frac{5}{2}\Gamma T_{e,i}^{SOLPS}\right) \Big/ n^{EXP} \nabla T_{e,i}^{EXP} \qquad (1)$$

where Γ, q_e, and q_i are the particle, electron heat and ion heat fluxes, and the superscripts SOLPS and EXP refer to quantities that are taken from the code and from measurements, respectively. The experimental profiles are modified hyperbolic tangent fits to the measured data points [18], which have been used previously in stability analysis [14]. The simulation is rerun using the updated transport coefficients, and this process is repeated until a satisfactory fit is achieved. The position of the profiles with respect the separatrix is constrained using measurements of the heat flux incident on the divertor plates [19], obtained with infrared cameras [20]. The upstream profiles are shifted in the radial direction (within the typical uncertainty of the separatrix location), to maintain agreement in the peak heat flux from measurement and modeling.

3. Results of the modeling

3.1. Matching midplane profiles

This fitting procedure gives a good match in the midplane profiles between measurement and modeling for the pre-lithium case (Fig. 1). The electron profiles show a clear pedestal structure typical of the H-mode edge, with a change in the density and temperature gradients near $\psi_N \sim 0.95$ giving a demarcation of the pedestal top. The ion temperature profile does not show a clear pedestal, partly owing to a relatively high value at the separatrix. The heat flux from measurements and modeling is also shown (the profiles are shifted in the plot to align the position of the peak from measurement and simulation, to account for uncertainty in the reconstructed outer strike point position). The radial decay length is somewhat shorter in the code results than is measured. The profile shape could be better reproduced using poloidally varying transport coefficients; in the present work poloidally constant coefficients are used, since insufficient data is available to constrain such a dependence.

Good agreement between modeled and measured midplane profiles is also achieved in the post-lithium case (panels e–h). With lithium, the electron temperature and density gradients remain fairly strong throughout the simulation region, without the break in gradient evident in the previous case; this makes the pedestal top more difficult to define. For this case, the ion temperature measurement is not available outside $\psi_N \sim 0.95$. To fill in the data, the same SOL profile is used as in the pre-lithium case, and is connected to the measured data as evident from the modeled profiles.
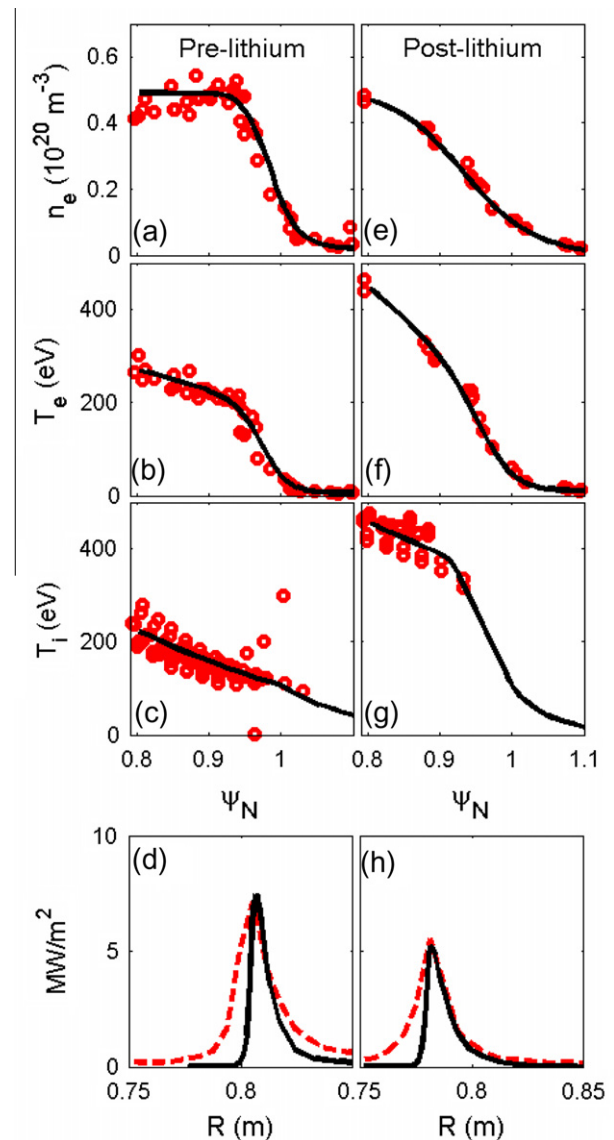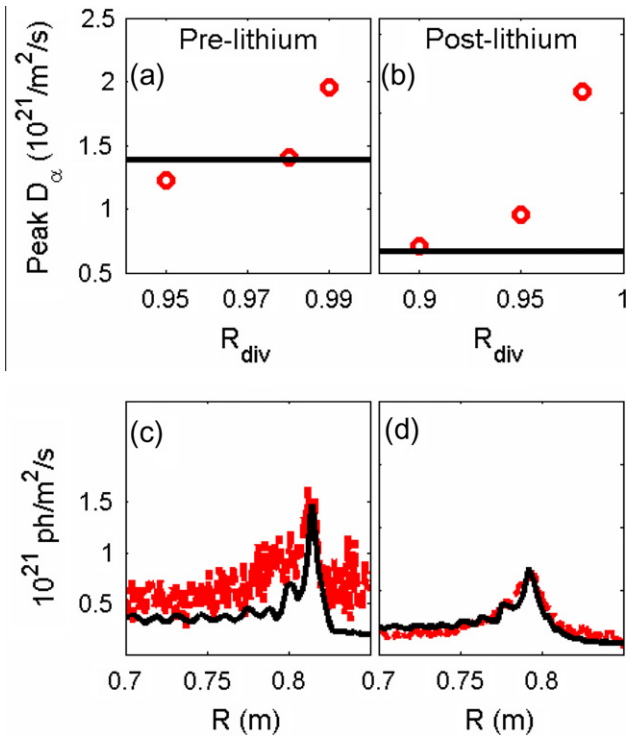

Fig. 1. Measured (red circles) and modeled (black lines) profiles of: (a) n_e, (b) T_e, (c) T_i, and (d) divertor heat flux for pre-lithium discharge; (e)–(h) corresponding plots for post-lithium case. (For interpretation of the references to colour in this figure legend, the reader is referred to the web version of this article.)

Since the implied pedestal and steep gradient are not directly measured, ion heat transport is not emphasized here. The divertor heat flux profile in the post-lithium case shows an improved fit of the decay length into the SOL, although the decay on the private flux region (PFR) side is again sharper than measurement indicates. It should be noted that some uncertainty exists in the magnitude of the heat flux, since lithium coatings may change the emissivity of the divertor surface, which is unaccounted for in the interpretation of the IR camera data. This is also true for the peak value used to constrain the separatrix position, although it can be hoped that near the peak heat flux, the lithium layer would be quickly eroded so that the emissivity change is less of an issue.

3.2. Matching D_α changes with lithium conditioning

Calibrated measurements of the D_α emission [21] on the outer divertor are used to constrain the value of the particle recycling coefficient R_{div} on the divertor targets used in the modeling (similar measurements for the inner divertor are not available). The pro-

Fig. 2. Peak modeled D_α brightness vs divertor recycling coefficient for (a) pre- and (b) post-lithium cases (horizontal lines indicate measured values). Measured (red) and modeled (black lines) D_α profile for (c) pre- and (d) post-lithium cases using best-fit R_{div}. (For interpretation of the references to colour in this figure legend, the reader is referred to the web version of this article.)

file fitting procedure described above is repeated for a series of simulations, with varying R_{div} (the recycling coefficient is set to unity at surfaces outside the divertor), yielding a new set of transport coefficients for each case. From each simulation, the calculated D_α emissivity is integrated along the lines-of-sight of the D_α camera installed on NSTX. The "best fit" recycling coefficient is taken to be the value of R_{div} for which the peak D_α brightness from modeling matches that from experiment (Fig. 2). This method gives $R_{div} \sim 0.98$ for the pre-lithium case, indicating a fairly high-recycling surface, with some wall-pumping as has been inferred from particle balance analysis of other NSTX discharges [22]. For the post-lithium case, a much lower value of $R_{div} \sim 0.9$ is obtained, confirming the expectation that the lithium acts as a pump for the incident deuteron flux. This method for determining R_{div} is somewhat over-restrictive, since it has been observed previously that the modeled D_α brightness typically only matches measurements to within roughly a factor of two [23]. The reduction in recycling inferred here should be considered as a means to evaluate the change in recycling, with less significance given to the absolute value of R_{div} in either case.

The profiles of the simulated and measured D_α brightness using the best-fit values of R_{div} are shown in Fig. 2. As was observed in the heat flux, in the pre-lithium case the D_α profile shows a sharper radial decay on the SOL side than is measured. The post-lithium modeling results show better agreement with experiment across the profile, on both the SOL and PFR sides.

3.3. Transport modifications with lithium coatings

The particle and electron thermal diffusivities from the interpretive modeling (Fig. 3) reflect the altered pedestal structure observed with lithium coatings (these coefficients correspond to the
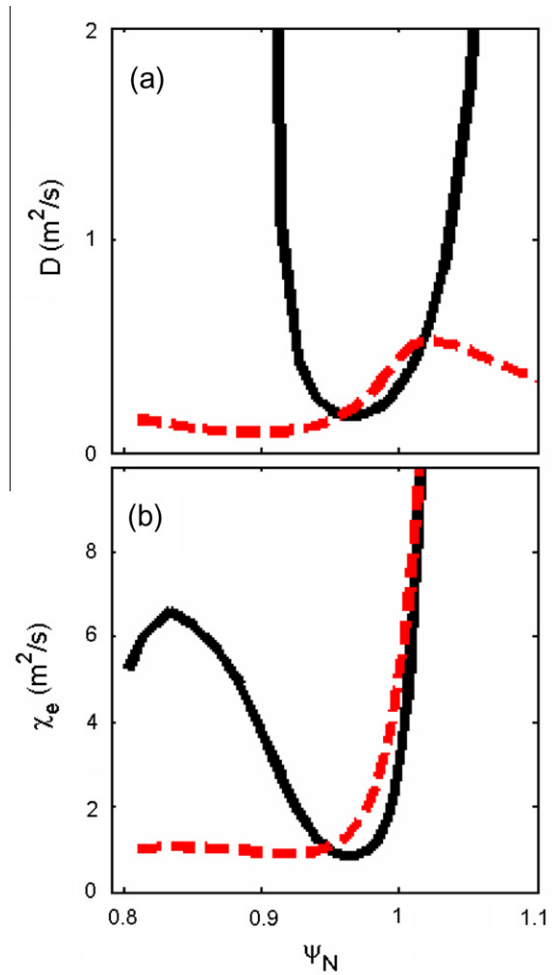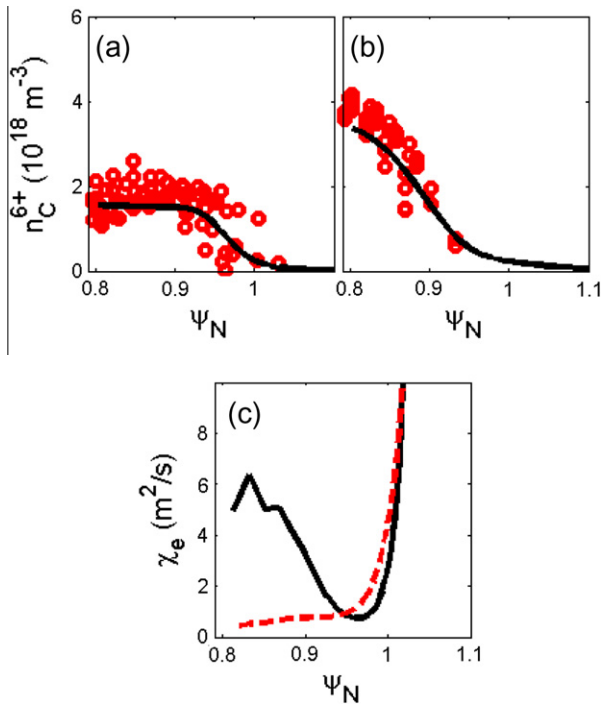

Fig. 3. Calculated (a) particle and (b) electron thermal diffusivity for pre- (solid black) and post-lithium (dashed red) discharges. (For interpretation of the references to colour in this figure legend, the reader is referred to the web version of this article.)

profiles shown in Fig. 1; the best-fit values of R_{div} were used). In the pre-lithium case these show a barrier structure, with a local minimum in D and χ_e corresponding to the steep gradient region just inside the separatrix. Between $\psi_N \sim 0.95$ and the separatrix, D and χ_e are similar in the pre- and post-lithium discharges, with comparable minimum values in the barrier region ($D \sim 0.2$, $\chi_e \sim 1.0$ m^2/s). Inside of $\psi_N \sim 0.93$, however, the transport is quite different with lithium coatings: in this case, the low values of D and χ_e observed in the barrier region extend all the way to the inner boundary of the simulation ($\psi_N \sim 0.8$). Thus, the change to the transport appears to be a widening of the edge transport barrier with lithium coatings, rather than reduced transport within the barrier itself. This modification, combined with reduced particle and heat fluxes with lithium (due to reduced input power and recycling), results in pedestal profiles that are much broader than the pre-lithium case, with a reduced density gradient.

3.4. Effects of including carbon in the modeling

The effect of impurities on the edge transport has been considered by including carbon in a set of simulations. This species is included rather than lithium since measurements show that with lithium coatings, carbon is the dominant plasma impurity, with concentrations as much as two orders of magnitude higher than lithium [11] (other 2-D modeling including lithium has been per-

Fig. 4. Measured (red circles) and modeled (solid black) carbon density for (a) pre- and (b) post-lithium discharges. Corresponding profiles of (c) electron thermal diffusivity for pre- (solid black) and post-lithium (dashed red) plasmas. (For interpretation of the references to colour in this figure legend, the reader is referred to the web version of this article.)

formed using the UEDGE code [24]). Carbon is produced by sputtering at the PFC surfaces, with a chemical sputtering yield of 2% assumed. A species independent diffusivity is used, based on the profile fitting procedure described above. For carbon, an inward convective velocity is added, motivated by the inward neoclassical convection that has been predicted and measured in the H-mode pedestal of other tokamaks [25] (a rigorous calculation of the neoclassical transport is not performed, and is left to future research). This velocity is spatially constant and independent of charge state, with a magnitude set so that the carbon concentration in the simulation agrees with measurement.

In the pre-lithium discharge, an inward velocity of 20 m/s is sufficient to match the measured C^{6+} density (Fig. 4), and with lithium coatings a comparable value of 15 m/s is found. The inclusion of carbon does affect the particle transport coefficients, with the D required to match the upstream density being somewhat higher in order to provide the outward particle flux needed to offset the inward convection. However, the interpretation of this is difficult, since the convection–diffusion model used here is an ansatz not based directly on theory, and the existing data does not allow the separate determination of the values of D and v (the coefficients discussed in Section 3.3 should be considered "effective" diffusivities, with no attempt made to differentiate between diffusion and convection). Heat transport, on the other hand, is more easily interpreted since no new convective terms are added. The general results from the deuterium-only simulations are not affected by

the inclusion of carbon (Fig. 4). As before, the effect of lithium coatings is to broaden the region with low transport, with χ_e being reduced by a factor of 4–6 inside $\psi_N \sim 0.9$ compared to the reference discharge, and remaining low to the inner boundary of the simulation.

4. Summary and conclusions

2-D modeling has been performed of two NSTX discharges, one with boron-coated carbon PFCs, the other with lithium coatings. The modeling is constrained by measurements of the midplane density and temperature profiles, and the divertor D_α and heat flux. The method used to fit the data allow the determination of the cross-field transport and divertor recycling coefficients.

The results show that lithium coatings reduce R_{div} from 0.98 to 0.9. However, this alone is insufficient to account for the relaxation of the pedestal gradients. Rather, the transport coefficients show a modified structure, with a widening of the edge transport barrier in both the electron heat and particle channels. This, combined with the reduced radial fluxes in the discharge with lithium, result in much broader pedestal profiles, which have been shown to result in the observed suppression of ELMs. While these conclusions are based on pure deuterium simulations, the feature of a widened transport barrier is not affected by the inclusion of carbon impurities. Future research will explore the causes behind these transport modifications, including possible changes to the turbulence believed to be governing transport near the pedestal top.

Acknowledgements

References

[1] R.F. Mattas et al., Fusion Eng. Des. 49–50 (2000) 127.
[2] Y. Hirooka et al., Nucl. Fusion 46 (2006) S56.
[3] L.E. Zakharov et al., Fusion Eng. Des. 72 (2004) 149.
[4] R. Majeski et al., Phys. Rev. Lett. 97 (2006) 075002.
[5] D.K. Mansfield et al., Nucl. Fusion 41 (2001) 1823.
[6] Y. Hirooka et al., J. Nucl. Mater. 390–391 (2009) 502.
[7] R. Kaita et al., Phys. Plasmas 14 (2007) 056111.
[8] M. Ono et al., Nucl. Fusion 40 (2000) 557.
[9] H. Kugel et al., J. Nucl. Mater. 363–365 (2007) 791.
[10] H. Kugel et al., Phys. Plasmas 15 (2008) 056118.
[11] M.G. Bell et al., Plasma Phys. Control. Fusion 51 (2009) 125054.
[12] R. Maingi et al., Nucl. Fusion 45 (2005) 1066.
[13] D.K. Mansfield et al., J. Nucl. Mater. 390–391 (2009) 764.
[14] R. Maingi et al., Phys. Rev. Lett. 103 (2009) 075001.
[15] R. Schneider et al., Contrib. Plasma Phys. 46 (2006) 3.
[16] B. Braams et al., Contrib. Plasma Phys. 36 (1996) 276.
[17] D. Reiter et al., Fusion Sci. Technol. 47 (2005) 172. <http://www.eirene.de>.
[18] R.J. Groebner, T.H. Osborne, Phys. Plasmas 5 (1998) 1800.
[19] R. Maingi et al., J. Nucl. Mater. 363–365 (2007) 196.
[20] D. Mastrovito et al., Rev. Sci. Instrum. 74 (2003) 5090.
[21] V.A. Soukhanovskii et al., Rev. Sci. Instrum. 74 (2003) 2094.
[22] V.A. Soukhanovskii et al., J. Nucl. Mater. 313–316 (2003) 573.
[23] A.V. Chankin et al., Plasma. Phys. Control. Fusion 48 (2006) 839.
[24] R.D. Smirnov et al., Contrib. Plasma Phys. 50 (2010) 299.
[25] T. Putterich, et al., in: 36th EPS Conf. on Plasma Phys., Sofia, Bulgaria, June 29–July 3, 2009, ECA vol. 33E, P-1.158.